Evidence of Dirac Quantum Spin Liquid in $YbZn_2GaO_5$

Rabindranath Bag,[1] Sijie Xu,[1] Nicholas E. Sherman,[2,3] Lalit Yadav,[1] Alexander I. Kolesnikov,[4] Andrey A. Podlesnyak,[4] Eun Sang Choi,[5] Ivan da Silva,[6] Joel E. Moore,[2,3] and Sara Haravifard[1,7,*]

[1]*Department of Physics, Duke University, Durham, North Carolina 27708, USA*
[2]*Department of Physics, University of California, Berkeley, California 94720, USA*
[3]*Materials Sciences Division, Lawrence Berkeley National Laboratory, Berkeley, California 94720, USA*
[4]*Neutron Scattering Division, Oak Ridge National Laboratory, Oak Ridge, Tennessee 37831, USA*
[5]*National High Magnetic Field Laboratory and Department of Physics, Florida State University, Tallahassee, Florida 32310, USA*
[6]*ISIS Neutron and Muon Source, Rutherford Appleton Laboratory, Didcot, Oxfordshire OX11 0QX, United Kingdom*
[7]*Department of Mechanical Engineering and Materials Science, Duke University, Durham, North Carolina 27708, USA*

(Received 19 January 2024; revised 11 September 2024; accepted 13 November 2024; published 30 December 2024)

The emergence of a quantum spin liquid (QSL), a state of matter that can result when electron spins are highly correlated but do not become ordered, has been the subject of a considerable body of research in condensed matter physics [1,2]. Spin liquid states have been proposed as hosts for high-temperature superconductivity [3] and can host topological properties with potential applications in quantum information science [4]. The excitations of most quantum spin liquids are not conventional spin waves but rather quasiparticles known as spinons, whose existence is well established experimentally only in one-dimensional systems; the unambiguous experimental realization of QSL behavior in higher dimensions remains challenging. Here, we investigate the novel compound $YbZn_2GaO_5$, which hosts an ideal triangular lattice of effective spin-1/2 moments with no detectable inherent chemical disorder. Thermodynamic and inelastic neutron scattering measurements performed on high-quality single crystal samples of $YbZn_2GaO_5$ exclude the possibility of long-range magnetic ordering down to 0.06 K, demonstrate a quadratic power law for the specific heat and reveal a continuum of magnetic excitations in parts of the Brillouin zone. Both low-temperature thermodynamics and inelastic neutron scattering spectra suggest that $YbZn_2GaO_5$ is a $U(1)$ Dirac QSL with spinon excitations concentrated at certain points in the Brillouin zone. We advanced these results by performing additional specific heat measurements under finite fields, further confirming the theoretical expectations for a Dirac QSL on the triangular lattice of $YbZn_2GaO_5$.

DOI: 10.1103/PhysRevLett.133.266703

Introduction—Anderson's proposal in 1973 ignited a surge of both experimental and theoretical efforts to identify the origins and properties of quantum spin liquid (QSL) states [5]. QSLs are exotic states of matter that remain disordered due to strong quantum fluctuations even at ultralow temperatures [1,2,6]. Despite significant experimental efforts, the unambiguous realization of a QSL state in the real world remains a challenge. In recent years, two-dimensional triangular lattice systems with rare-earth ions carrying effective spin-1/2 moments have presented promising opportunities in realizing QSL states, given the presence of spin-orbit coupling, crystal electric fields, and strong quantum fluctuations. Among these systems, the Yb-based $YbMgGaO_4$ has been intensively studied due to the absence of magnetic ordering and the observed continuumlike inelastic neutron scattering (INS) spectra, making it a promising candidate for QSL [7–13]. However, the presence of chemical disorder in $YbMgGaO_4$, caused by the inherently mixed occupancies of magnesium and gallium atoms on the same crystallographic site, has made the interpretation of the results challenging [12–14]. Specifically, a theoretical study suggests that the chemical disorder may imitate the continuous INS spectra [12]. Further studies on a sister compound, $YbZnGaO_4$, have proposed the presence of a spin-glass ground state attributed to the coexistence of chemical disorder and quantum fluctuation [15]. Therefore, eliminating or suppressing chemical disorder and accessing the intrinsic physics of an ideal triangular lattice of effective spin-1/2 moments is highly desired. As such, a potential candidate for hosting a QSL state is another class of Yb-based triangular lattice rocksalt-type compounds that do not have significant intrinsic chemical disorder: $AYbX_2$ (A = Li, Na, K, Rb, Cs, and X = O, S, Se) [16–26]. Nevertheless, the task of obtaining high-quality single-crystal samples for this particular family has posed significant challenges. As a result, most of the reported results have been derived from powder samples or small single crystals, rendering the interpretation of data quite challenging.

*Contact author: sara.haravifard@duke.edu

Furthermore, it is worth noting that in this compound family, the interlayer Yb-Yb distance is relatively shorter, which introduces a more three-dimensional magnetic structure. Therefore, the key to unlocking the mystery of the QSL state in these systems hinges on creating and synthesizing single-crystal samples for a new category of Yb-based triangular lattice compounds. These compounds should lack significant intrinsic chemical disorder and showcase a more two-dimensional magnetic structure.

To that end, we present a new Yb-based compound, $YbZn_2GaO_5$, that features an ideal triangular lattice of effective spin-1/2 moments without detectable intrinsic chemical disorder. Experiments aimed at elucidating the nature of the possible triangular lattice QSL in $YbZn_2GaO_5$ are of great importance. Thus, we grew a large and high-quality single crystal of $YbZn_2GaO_5$ (see Fig. S1 [27]) using the optical floating-zone technique to facilitate such experiments (see Appendix A). Our specific heat measurements indicate that at ultralow temperatures (see Appendix D), the specific heat displays a $\sim T^2$ dependence, indicating a $U(1)$ Dirac QSL behavior [28,29]. Additionally, we show that the field-induced T-linear component of the specific heat is proportional to the applied magnetic field, further confirming that the ground state of $YbZn_2GaO_5$ is best described with $U(1)$ Dirac QSL [28]. In addition to the specific heat measurements, we conducted INS investigation on $YbZn_2GaO_5$ which reveals gapless, continuumlike spectra at the high-symmetry M and K points, but not throughout the Brillouin zone, and in particular not at the Γ point. This particular pattern of low-energy spinon excitations is expected for the $U(1)$ Dirac QSL phase [30,31] and not for a spinon Fermi surface state. Hence the specific heat scaling and INS spectra independently are best explained by low-energy spinon excitations with a Dirac-like spectrum.

Results and discussion—Before discussing the results further, we would like to review briefly the key signatures that differentiate a spinon Fermi surface state from a $U(1)$ Dirac spin liquid. First, let us start with the spinon Fermi surface state. In such a state, the low-temperature specific heat is predicted to scale as $\sim T$ [32] at the mean-field level, possibly becoming $T^{2/3}$ if emergent gauge fluctuations dominate. As for the spectrum, mean-field theory predicts a V-shaped spectrum near the Γ point and gapless excitations throughout the entire Brillouin zone [6,10,33]. These signatures have been observed in $YbMgGaO_4$ [10,34] and $NaYbSe_2$ [21]. For the $U(1)$ Dirac spin liquid, the specific heat is expected to scale as $\sim T^2$ because of the Dirac nodes [28,35]. The low-energy theory on the triangular lattice is quantum electrodynamics (QED_3) with four Dirac fermions ($N_f = 4$), which predicts gapless excitations at both the M and K wave vectors [36]. The main signature to distinguish this from a spinon Fermi surface state is the presence of a gap away from these points, such as near the Γ point, as observed in recent simulations of the $J_1 - J_2$ Heisenberg model on the triangular lattice [30,31,37].

Returning to the discussion of $YbZn_2GaO_5$, we demonstrate in Fig. 1(a) the hexagonal crystal structure of $YbZn_2GaO_5$, with the space group $P6_3mmc$. This is in contrast to $YbMgGaO_4$ and $YbZnGaO_4$ which crystallize in the $R\bar{3}m$ space group. Within the $P6_3mmc$ space group of $YbZn_2GaO_5$, distinctive Wyckoff positions are allocated for gallium and zinc. Consequently, $YbZn_2GaO_5$ exhibits no observable intrinsic chemical site mixing. The phase purity of our sample is confirmed through a Rietveld refinement analysis performed on the powder x-ray diffraction pattern obtained from a crushed $YbZn_2GaO_5$ single crystal (see Fig. S1 [27]). We further performed the single-crystal x-ray diffraction measurement (see Appendix B) on $YbZn_2GaO_5$ crystal and observed no chemical disorder within the limit of our experimental accuracy (see Table S1 [27]). In order to further confirm this, we also performed high-resolution neutron powder diffraction measurements on $YbZn_2GaO_5$ (see Appendix F). These results also show no signature of detectable site mixing in this system. This is an important observation since unlike their similar x-ray cross sections, the neutron cross sections for Zn and Ga differ by a factor of 1.65 (see Fig. S2), making it easier to detect the possible chemical site mixing. It is noteworthy to add that in $YbZn_2GaO_5$, an additional nonmagnetic Zn-O layer is introduced along the crystallographic c direction, which increases the distance between magnetic Yb-O planes from 8.38 Å ($YbZnGaO_4$) to 10.98 Å, enhancing the two-dimensionality and quantum fluctuations in this compound compared to previously reported Yb-based triangular lattice QSL candidates [11,15–17]. The nearest neighbor Yb^{3+} ions are arranged in a perfect triangular pattern with a distance of 3.37 Å between them, as illustrated in Fig. 1(b). This distance is comparable to that in the previously reported Yb-based triangular lattice compounds proposed to host QSL state [7,8].

We illustrate in Fig. 1(c) the temperature-dependent magnetic susceptibility data collected on the single crystal of $YbZn_2GaO_5$ along both directions parallel and perpendicular to the crystallographic c axis, in the presence of an applied magnetic field of 0.01 T (see Appendix E). The inset of Fig. 1(c) highlights the low-temperature susceptibility region down to 0.3 K, confirming the absence of magnetic ordering down to this temperature. The inverse magnetic susceptibility data are fitted to Curie-Weiss law: $1/\chi = (T-\theta_{CW})/C$, (where θ_{CW} is the Curie-Weiss temperature, and C is the Curie constant) at two different temperature regimes. The obtained effective moment ($\mu_{eff} \simeq 4.36\ \mu_B$) at a high-temperature range agrees with the expected theoretical value of free Yb^{3+} ion ($\simeq 4.54\ \mu_B$). The Curie-Weiss temperatures obtained for $YbZn_2GaO_5$ in the low-temperature range (5–15 K) are slightly higher ($\theta_{CW,\parallel} = -3.77$ K and $\theta_{CW,\perp} = -5.22$ K) than those of $Yb(Mg,Zn)GaO_4$ [7,8,10,15,38]. This observation suggests a stronger antiferromagnetic coupling between Yb^{3+} ions in $YbZn_2GaO_5$. The

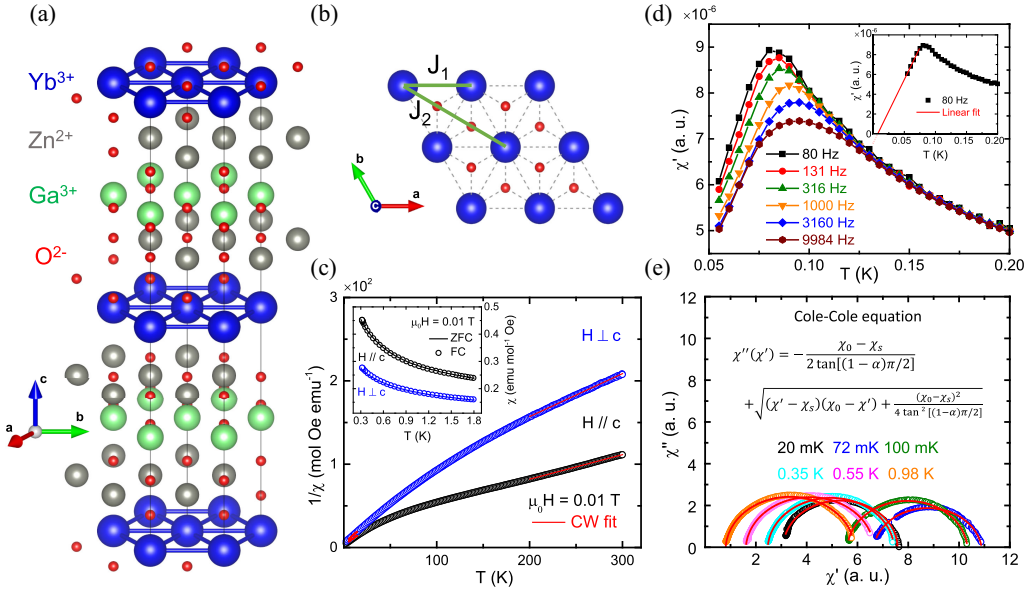

FIG. 1. Crystal structure and magnetic susceptibility. (a) Crystal structure of $YbZn_2GaO_5$; Yb-O planes are well separated by nonmagnetic Zn-O, Ga-O, and Zn-O layers along crystallographic c direction. (b) The Yb^{3+} (blue sphere) forms a triangular lattice. The nearest neighbor couplings J_1 and next-nearest neighbor couplings J_2 are shown by green solid lines. (c) The inverse magnetic susceptibility, $1/\chi$ (H$\|c$ and H$\perp c$) data collected on single-crystal sample of $YbZn_2GaO_5$ from 2 to 300 K. The red solid lines are the Curie-Weiss (CW) fit at the low-temperature range from 5–15 K and at high-temperature range from 200–300 K. The inset shows no splitting between zero-field-cooling (ZFC) and field cooling (FC) magnetic susceptibility data of $YbZn_2GaO_5$ crystal down to 0.3 K. The measurements were conducted under an applied magnetic field of 0.01 T parallel and perpendicular to crystallographic c direction. (d) Temperature dependence of the real part of the ac susceptibility. The inset displays a linear fit of the data at 80 Hz, ranging from 0.055 to 0.08 K. Our linear fit extrapolates to the origin within the uncertainty range. (e) Cole-Cole plot (Argand diagram) at different temperatures. The data were collected at a series of frequencies in the range of 10 to 3000 Hz. Data at each fixed temperature were individually fitted to the Cole-Cole equation shown in the plot. Our fit yields Cole-Cole coefficient α of 0.005(2), 0.080(1), 0.041(3), 0.033(1), 0.032(2), and 0.030(2), for 20 mK, 72 mK, 100 mK, 0.35 K, 0.55 K, and 0.98 K, respectively.

collected isothermal magnetization data along both directions up to 14 T of the applied magnetic field provides anisotropic Landé g factors of $g_{\|} \simeq 3.44$ and $g_{\perp} \simeq 3.04$ (see Fig. S1f).

As proposed in previous studies on $Yb(Mg, Zn)GaO_4$, one plausible explanation for the absence of long-range magnetic ordering could be that the ground state is a spin glass [15]. In the spin-glass state, the spins are locked into a static, short-range ordered state below the freezing temperature (T_f) due to competing exchange interactions [39]. Detection of the spin-glass state typically involves ac-susceptibility measurements. We conducted ac-susceptibility measurements on $YbZn_2GaO_5$ single-crystal samples (see Appendix C). In Fig. 1(d), the real part of the ac susceptibility (χ') at 80 Hz reveals a maximum at $T_f \approx 0.082$ K, at a slightly lower value compared to that observed in $Yb(Mg, Zn)GaO_4$ [15]. The observed peak exhibits a small frequency-dependent behavior, shifting slightly toward higher temperatures for low frequency regime. We attribute this behavior to the freezing of the orphan spins present in the small impurity phase rather than the spin-glass nature of the ground state for $YbZn_2GaO_5$. To further elaborate on this, we show in the inset of Fig. 1(d) the interpolation of lowest measured frequency (80 Hz) at the zero temperature limit, suggesting that the susceptibility passes through origin and is linear as a function of temperature in this regime. This is in agreement with our expectation for a Dirac quantum spin liquid state [28,35] and implies that $YbZn_2GaO_5$ is unlikely to exhibit a spin-glass ground state. Furthermore, the spin-glass scenario is ruled out by the Cole-Cole analysis shown in Fig. 1(e), where χ'' versus χ' is plotted as frequency sweeps at fixed temperatures. The Cole-Cole plot illustrates the distribution of relaxation times, characterized by the fitting parameter α. A perfect semicircle corresponds to $\alpha = 0$ and implies a single relaxation time, while a highly flattened semicircle corresponds to $\alpha \to 1$, indicating a broad distribution of relaxation times [40]. In a typical spin glass, one would anticipate a broad spectrum of relaxation times [39,41]. However, in $YbZn_2GaO_5$, the obtained α falls within the range of 0.005 to 0.08, consistent with a single relaxation time at temperatures both below and above the peak position at T_f. Remarkably, even at the base temperature of 0.02 K, which is significantly below T_f, the smallest α value of 0.005 was obtained. These observations exclude the possibility of the spin-glass scenario and suggest that the ground state of $YbZn_2GaO_5$ remains dynamic down to 0.02 K.

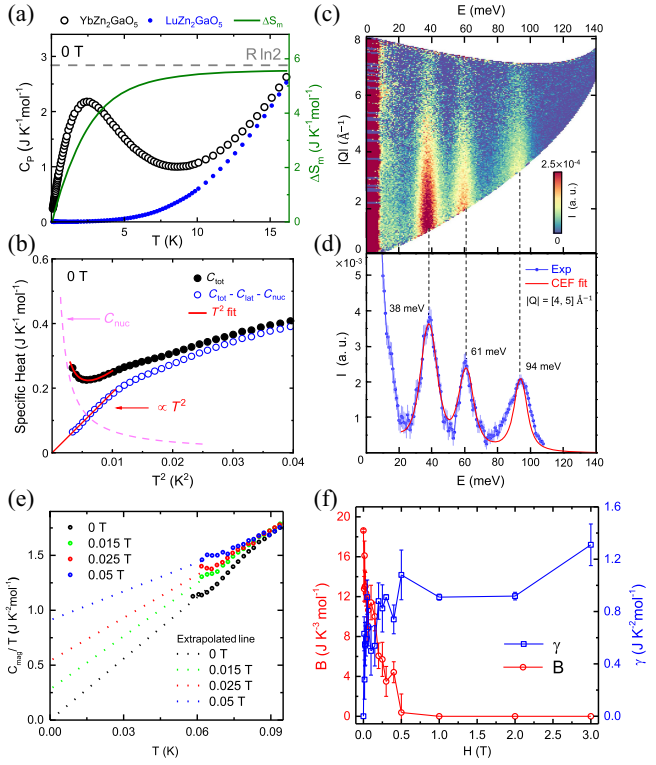

FIG. 2. Specific heat and crystal electric field levels. (a) Specific heat data of $YbZn_2GaO_5$ single crystal and $LuZn_2GaO_5$ powder sample collected under zero field and down to 0.06 K are shown. The calculated magnetic entropy (right y axis) of $YbZn_2GaO_5$ saturates to Rln2, indicating the effective spin-1/2 ground state. (b) Specific heat vs T^2 plot: low-temperature total specific heat ($C_{\rm tot} = C_{\rm lat} + C_{\rm nuc} + C_{\rm mag}$) shows an upturn below 0.1 K. Using an isostructural nonmagnetic $LuZn_2GaO_5$ and a fitted Schottky model ($C_{\rm nuc} \simeq AT^{-2}$), the lattice and nuclear contributions were removed. The magnetic specific heat data ($C_{\rm mag}$) after subtraction is presented as open circles and fitted with a solid red straight line that exhibits a quadratic T dependence ($C_{\rm mag} \simeq BT^2$). The quadratic T-dependence fit yields an adjusted R-square value of 0.9583, indicating noticeable agreement between the model and experimental data. The T^2 dependence of magnetic specific heat data for $T \to 0$ implies $YbZn_2GaO_5$ is a $U(1)$ Dirac QSL candidate. (c) INS spectra of $YbZn_2GaO_5$ reveal three crystal electric field (CEF) bands. The phononic contribution is subtracted using an isostructural nonmagnetic sample $LuZn_2GaO_5$. (d) The single-ion CEF fitting shows energy levels at 38, 61, and 94 meV. The vertical error bars indicate statistical errors of 1 standard deviation. (e) The magnetic specific heat ($C_{\rm mag}/T$) under finite applied magnetic field plotted and extrapolated (dashed line) down to 0 K suggesting the Dirac QSL behavior, as $C_{\rm mag}/T$ is linearly going up with magnetic field [28]. (f) The field dependence of B and γ fit parameters along with the error bars, extracted from the magnetic contribution of the specific heat modeled by $C_{\rm mag} \simeq BT^2 + \gamma T$.

Theoretical models at the mean-field level predict Dirac QSL behavior at low temperatures, specifically when $k_BT \ll \chi J$, with χ representing the magnitude of the self-consistent mean-field parameter [28]. According to this theory one expects specific heat $\propto T^2$ law due to the Dirac nodes. We show in Fig. 2(a) zero-field specific heat measurement performed on a $YbZn_2GaO_5$ single-crystal sample down to 0.06 K, confirming the absence of any long-range magnetic ordering. The contribution of phonons is subtracted using the isostructural nonmagnetic sample of $LuZn_2GaO_5$. In Fig. 2(b), we highlight the low-temperature behavior of the specific heat data to comply with the $k_BT \ll \chi J$ condition. The specific heat of $YbZn_2GaO_5$ at this temperature range has multiple contributions denoted by $C_{\rm tot} = C_{\rm lat} + C_{\rm nuc} + C_{\rm mag}$. $C_{\rm lat}$ represents the lattice (phononic) contribution that is negligible below 0.1 K. $C_{\rm nuc}$ accounts for the nuclear Schottky contribution due to the hyperfine splitting of the nuclear energy levels resulting from the interaction between nuclear spins and electrons [42]. The nuclear contribution ($C_{\rm nuc} \simeq AT^{-2}$) is subtracted by fitting the specific heat data below 0.1 K and the fitting coefficient value [$A = 6.72(4) \times 10^{-4}$ JK mol^{-1}] is consistent with that reported for other Yb-based compounds [22]. Interestingly for $YbZn_2GaO_5$ the subtracted magnetic specific heat data ($C_{\rm mag}$) displays a $\propto T^2$ dependence [red solid straight line in Fig. 2(b)] with a coefficient of $B = C_{\rm mag}/T^2 = 18.6(1)$ JK^{-3} mol^{-1} below 0.1 K. As discussed above, this is in agreement with the proposed Dirac QSL behavior [28]. We also attempted to fit the magnetic specific heat data with a linear dependence ($C_{\rm mag} \propto T$), but this fitting approach did not provide a satisfactory result (see Fig. S4). Therefore, the magnetic specific heat data exhibiting a $\propto T^2$ dependence for T $\to$ 0 and the lack of any long-range magnetic ordering down to the lowest temperature of 0.06 K imply that the ground state of $YbZn_2GaO_5$ is likely a $U(1)$ Dirac QSL [28,35].

Another hallmark of Dirac spinons is their behavior in a Zeeman field, where the specific heat displays a linear increase with the applied field strength. In other words, at $k_BT \ll \mu_BH$, Dirac spinons are theorized to form a Fermi pocket where the magnetic field strength correlates directly with the pocket's radius. To explore this phenomena further, we measured the specific heat of $YbZn_2GaO_5$ under various finite magnetic fields. To test this prediction, we gathered specific heat data at magnetic field strengths of 0.01 T, 0.015 T, 0.025 T, and 0.05 T, incrementing the temperature gradually. The results, illustrated in Fig. 2(e), support the theoretical framework, showing a linear rise in ($C_{\rm mag}/T$) as the magnetic field strength increases. This observed behavior stems from the splitting and vertical shift of Dirac nodes, which leads to a finite density of states directly proportional to the field strength. Detailed specific heat results under different magnetic fields and a comparison between experimental fit parameters and theoretical predictions are presented in Fig. S5 [27].

To provide further insight into the behavior of the specific heat as function of field, we model the magnetic contribution of the specific heat by $C_{\rm mag} \simeq BT^2 + \gamma T$. We show in Fig. 2(f) the field dependence of the extracted B

and γ parameters. The results obtained for B confirm the T^2 behavior of the specific heat at zero field, while the values extracted for γ demonstrate a linear increase in specific heat as a function of magnetic field. The field-dependent ratio of γ and B coefficients is also consistent with theoretical expectations (see Supplemental Material [27]), further confirming that the ground state of $YbZn_2GaO_5$ is best described by $U(1)$ Dirac QSL.

To gain deeper insights into the dynamics of $YbZn_2GaO_5$, we conducted an INS experiment using a high-purity powder sample at 5 K, as depicted in Figs. 2(c) and 2(d). The single-ion crystal electric field (CEF) fitting results revealed three distinct crystal field excitations at 38, 61, and 94 meV, which agree with those observed in other previously reported Yb-based triangular lattice systems [14,17,21,43–45]. Based on our analysis of the CEF levels, we have determined that the first excited state of $YbZn_2GaO_5$ is separated from the ground state by a gap of over 441 K (38 meV). This suggests a Kramer's doublet ground state for the Yb^{3+} ions with an effective spin-1/2. Our CEF fitting scheme, which is consistent with the specific heat data, supports this conclusion. In particular, the calculated magnetic entropy of $YbZn_2GaO_5$ saturates at Rln2, indicating an effective spin-1/2 ground state, as shown in Fig. 2(a) (see Tables S2 and S3 for further details on the CEF fitting scheme).

It is important to note the observed broadening of the 94 meV CEF excitation band. Previous studies have linked broadening at 97 meV and the emergence of an additional band at 138 meV in $YbMgGaO_4$ to disorder [14]. However, broadening in CEF levels can also stem from various mechanisms in rare-earth-based compounds. For instance, Gaudet *et al.* [46] describe a shoulderlike feature in one of the CEF levels of $Ho_2Ti_2O_7$, which results from the hybridization of a nearby phonon mode with the CEF mode, forming a vibronic mode. Consequently, the shoulder observed at approximately 87.5 meV in our data does not necessarily suggest disorder. In $YbZn_2GaO_5$, phonon excitations up to approximately 90 meV were also observed in the INS data collected on the isostructural nonmagnetic compound $LuZn_2GaO_5$, which could potentially lead to the formation of vibronic bonds. Thus, we propose that the observed broadening may be attributed to CEF-phonon coupling, underscoring the need for further detailed investigation of this system using complementary techniques such as Raman spectroscopy [23,47].

Furthermore, we conducted INS experiments on a high-quality single crystal of $YbZn_2GaO_5$ (see Appendix G).

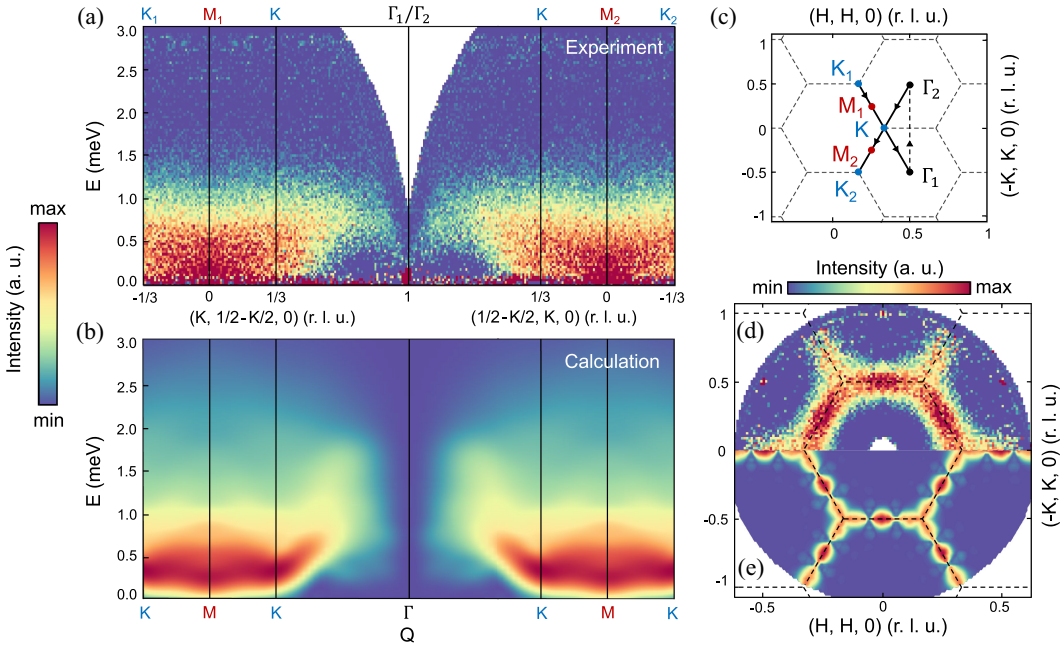

FIG. 3. Inelastic neutron scattering data under zero applied magnetic field. (a) Energy dependence of the magnetic excitation spectrum along high-symmetry points measured at 0.1 K. The background is subtracted using the high-temperature (45 K) spectrum (see Appendix G for details). The contour path travels along the high-symmetry points K_1-M_1-K-Γ_1/Γ_2-K-M_2-K_2, which is illustrated by the black solid curve in c. (b) Calculated spectrum using matrix product states for the $J_1 - J_2$ XXZ model on the triangular lattice, with $J_2/J_1 = 0.12$ and $\Delta = 1.35$ (see Appendix H for details). We use $J_1 \sim 0.5$ meV to adjust the scale of the y axis for better comparison of the experimental data. (c). A schematic of the high symmetry path used in a,b. The dashed lines show the boundary of the Brillouin zones. (d) Background-subtracted low energy slice of the magnetic excitation spectrum collected at 0.1 K. The energy integration range is [0.1, 0.3] meV. (e) The calculated spectrum of the $J_1 - J_2$ XXZ model with the same parameters as in b. We integrate the spectrum in the energy range [0.1, 0.3] meV for comparison with d.

These experiments were designed to probe the low-energy excitations of the material. An incident neutron energy of 3.32 meV was used and the excitation spectrum under zero field was collected at a base temperature of 0.1 K. Scans performed at a high temperature of 45 K were used for background subtraction (see Fig. S3). We show in Fig. 3(a) the scattering intensity as a function of energy transfer, with a path taken through the high-symmetry points of K_1-M_1-K-Γ_1/Γ_2-K-M_2-K_2, as illustrated in Fig. 3(c).

Additionally, a broad continuum extending over an energy scale of approximately 1.4 meV was observed, with the spectrum weight gradually decreasing at higher energy. We observed a clear gap in the spectra of $YbZn_2GaO_5$ near the Γ point, while the excitation appears to be remained gapless between M and K points within the instrumental energy resolution of approximately 0.06 meV, as shown in Fig. 3(a). We present in Fig. 3(b) the outcome of our theoretical calculation, which are based on the $J_1 - J_2$ XXZ model and use large-scale matrix product state simulations (see Appendix H section for details) [30]. These results demonstrate promising agreement with our experimental data, with $J_2/J_1 \sim 0.12$ and an anisotropy value of $\Delta \sim 1.35$ [see Fig. S6(b)].

Even though the energy of the neutrons is higher than that needed to access the Dirac behavior directly, they do observe a spectrum that is consistent with the $J_1 - J_2$ model in the regime in which the Dirac QSL is most likely the ground state. It is worth noting that on the triangular lattice, the energy scale of the spinons in $J_1 - J_2$ model is not the largest magnetic energy scale J_1, which is the nearest-neighbor interaction, because on the triangular lattice, the J_1 coupling alone would lead to long-ranged three-sublattice order. The second largest coupling seems to be a second neighbor J_2, based on linear-spin-wave fits at high magnetic fields for similar Yb-based triangular lattice compounds [21,30], and the spinon energy scale is then expected to depend on the dimensionless parameter J_2/J_1. From numerical calculations, there is a window of J_2/J_1 between long-ranged ordered phases and where the QSL state is predicted to emerge; reasonable values are J_2/J_1 between 0.06 and 0.12 [30,52]. Therefore, the energy scale of the zone-boundary spinon is expected to be much less than J_1, which is consistent with a significant contribution to the specific heat at low temperatures and also with the violations of T^2 behavior at above ~0.1 Kelvin.

In contrast to $YbZn_2GaO_5$, other reported Yb-based triangular systems, such as the delafossite material $NaYbSe_2$, display a continuum spectrum without a gap at all Q. This observation is consistent with a spinon Fermi surface state [21,33]. However, in $YbZn_2GaO_5$, the observed energy gap near Γ along with the continuum spectra observed at $Q = K$ and M are indicative of a $U(1)$ Dirac QSL state [30]. The thermodynamic measurements are consistent with this picture, as the magnetic specific heat data (C_{mag}) exhibits a $\propto T^2$ dependence for $T \to 0$ as well as $\propto T$ behavior as function of magnetic field, which are also indicative of a $U(1)$ Dirac QSL.

In Fig. 3(d), we demonstrate the experimental dispersion of the neutron scattering intensities through constant energy slice integrated from 0.1 to 0.3 meV. We observe that at low energy, spectral weights are localized at the edge of the Brillouin zone, with higher intensities at the M points than at the K points [see Fig. S6(a) for linear cut [27]]. As the energy increases, the difference in intensities between M and K points becomes less prominent, and the intensities disperse throughout the Brillouin zone, as shown in Fig. S7. Moreover, the theoretical calculations in Fig. 3(e) agree with our experimental observations in similar energy ranges. The agreement between theory and experiment suggests that INS spectra of $YbZn_2GaO_5$ are sufficiently well described by the $J_1 - J_2$ XXZ model without additional couplings. The presence of what appears to be gapless modes at K and M while having a gap near Γ strongly favors a $U(1)$ Dirac QSL ground state over either a spinon Fermi surface or the effects of disorder.

Conclusions—In conclusion, we have successfully synthesized and characterized high-quality single crystals of $YbZn_2GaO_5$, a Yb-based triangular lattice system that displays no observable intrinsic chemical disorder. Our ac-susceptibility measurements rule out the possibility of a spin-glass ground state. Furthermore, our specific heat measurements reveal a quadratic temperature dependence of the magnetic component at ultralow temperatures, as well as linear-T dependence as function of magnetic field, providing strong experimental evidence for the presence of a $U(1)$ Dirac QSL state on a triangular lattice in $YbZn_2GaO_5$. Additionally, our INS investigation of $YbZn_2GaO_5$ shows gapless, continuumlike spectra at the high-symmetry M and K points, but *not* at the Γ point, confirming the potential existence of a $U(1)$ Dirac QSL ground state in this material, and these experimental findings align well with theoretical interpretations. Consequently, we firmly believe that $YbZn_2GaO_5$ represents a highly promising candidate for the elusive $U(1)$ Dirac QSL, and we advocate for further exploration using a diverse range of theoretical and experimental techniques. Furthermore, we have recently uncovered a substantial correlation between the predicted Dirac spin liquid spectrum for the superconducting cuprate pseudogap [48] and the physical properties observed in our compound. This discovery shines a spotlight on the potential realization of a Dirac QSL in $YbZn_2GaO_5$, underscoring its significance within the field.

Acknowledgments—We would like to express our gratitude to Patrick A. Lee, Cristian D. Batista, and Sachith E. Dissanayake for their valuable contributions to our discussions. We are thankful to Chun-Hsing Chen and the X-Ray Core Laboratory of the Department of Chemistry at the University of North Carolina at Chapel Hill for their help with single-crystal x-ray diffraction measurements. Work performed at Duke University is supported by the U.S. Department of Energy, Office of Science, Office of Basic Energy Sciences, under Award No. DE-SC0023405. Work performed at the University of California, Berkeley, is

supported by the U.S. Department of Energy, Office of Science, National Quantum Information Science Research Centers, Quantum Science Center. N. S. is additionally supported by the Theory Institute for Materials and Energy Spectroscopies (TIMES) of the U.S. Department of Energy, Office of Basic Energy Sciences, under Contract No. DE-AC02-05CH11231. R. B. acknowledges the support provided by Fritz London Endowed Postdoctoral Research Fellowship. This research used resources of the Spallation Neutron Source at Oak Ridge National Laboratory, which is a DOE Office of Science User Facility. A portion of this work was performed at the National High Magnetic Field Laboratory, which is supported by National Science Foundation Cooperative Agreement No. DMR-2128556 and the State of Florida.

Data availability—The data that support plots and other findings in this Letter are available from the contact author upon reasonable request. The computer codes used to generate results are available from the contact author upon reasonable request.

Research conceived by S. H. Samples synthesized by S. X., R. B., and S. H. Magnetic measurements performed and analyzed by S. X., R. B., and S. H. Specific heat measurements performed and analyzed by S. X., R. B, and S. H. ac-susceptibility measurements performed and analyzed by S. X., R. B., E. S. C., and S. H. Neutron scattering measurements performed and analyzed by S. X., A. I. K., A. A. P, I. S., and S. H. Theoretical calculations performed by N. E. S. and J. E. M. Manuscript written by S. X., R. B., N. E. S., J. E. M., and S. H. All authors commented on the manuscript.

[1] L. Balents, Nature (London) **464**, 199 (2010).
[2] C. Broholm, R. Cava, S. Kivelson, D. Nocera, M. Norman, and T. Senthil, Science **367**, eaay0668 (2020).
[3] P. W. Anderson, Science **235**, 1196 (1987).
[4] A. Kitaev, Ann. Phys. (Amsterdam) **303**, 2 (2003).
[5] P. Anderson, Mater. Res. Bull. **8**, 153 (1973).
[6] L. Savary and L. Balents, Rep. Prog. Phys. **80**, 016502 (2016).
[7] Y. Li, H. Liao, Z. Zhang, S. Li, F. Jin, L. Ling, L. Zhang, Y. Zou, L. Pi, Z. Yang *et al.*, Sci. Rep. **5**, 16419 (2015).
[8] Y. Li, G. Chen, W. Tong, L. Pi, J. Liu, Z. Yang, X. Wang, and Q. Zhang, Phys. Rev. Lett. **115**, 167203 (2015).
[9] Y. Li, D. Adroja, P. K. Biswas, P. J. Baker, Q. Zhang, J. Liu, A. A. Tsirlin, P. Gegenwart, and Q. Zhang, Phys. Rev. Lett. **117**, 097201 (2016).
[10] Y. Shen, Y.-D. Li, H. Wo, Y. Li, S. Shen, B. Pan, Q. Wang, H. Walker, P. Steffens, M. Boehm *et al.*, Nature (London) **540**, 559 (2016).
[11] J. A. Paddison, M. Daum, Z. Dun, G. Ehlers, Y. Liu, M. B. Stone, H. Zhou, and M. Mourigal, Nat. Phys. **13**, 117 (2017).
[12] Z. Zhu, P. A. Maksimov, S. R. White, and A. L. Chernyshev, Phys. Rev. Lett. **119**, 157201 (2017).
[13] I. Kimchi, A. Nahum, and T. Senthil, Phys. Rev. X **8**, 031028 (2018).
[14] Y. Li, D. Adroja, R. I. Bewley, D. Voneshen, A. A. Tsirlin, P. Gegenwart, and Q. Zhang, Phys. Rev. Lett. **118**, 107202 (2017).
[15] Z. Ma *et al.*, Phys. Rev. Lett. **120**, 087201 (2018).
[16] M. M. Bordelon, E. Kenney, C. Liu, T. Hogan, L. Posthuma, M. Kavand, Y. Lyu, M. Sherwin, N. P. Butch, C. Brown, M. J. Graf, L. Balents, and S. D. Wilson, Nat. Phys. **15**, 1058 (2019).
[17] L. Ding, P. Manuel, S. Bachus, F. Grußler, P. Gegenwart, J. Singleton, R. D. Johnson, H. C. Walker, D. T. Adroja, A. D. Hillier, and A. A. Tsirlin, Phys. Rev. B **100**, 144432 (2019).
[18] M. M. Bordelon, C. Liu, L. Posthuma, P. M. Sarte, N. P. Butch, D. M. Pajerowski, A. Banerjee, L. Balents, and S. D. Wilson, Phys. Rev. B **101**, 224427 (2020).
[19] J. Guo, X. Zhao, S. Ohira-Kawamura, L. Ling, J. Wang, L. He, K. Nakajima, B. Li, and Z. Zhang, Phys. Rev. Mater. **4**, 064410 (2020).
[20] K. M. Ranjith, D. Dmytriieva, S. Khim, J. Sichelschmidt, S. Luther, D. Ehlers, H. Yasuoka, J. Wosnitza, A. A. Tsirlin, H. Kühne, and M. Baenitz, Phys. Rev. B **99**, 180401(R) (2019).
[21] P.-L. Dai *et al.*, Phys. Rev. X **11**, 021044 (2021).
[22] K. M. Ranjith, S. Luther, T. Reimann, B. Schmidt, P. Schlender, J. Sichelschmidt, H. Yasuoka, A. M. Strydom, Y. Skourski, J. Wosnitza, H. Kühne, T. Doert, and M. Baenitz, Phys. Rev. B **100**, 224417 (2019).
[23] Z. Zhang, X. Ma, J. Li, G. Wang, D. T. Adroja, T. P. Perring, W. Liu, F. Jin, J. Ji, Y. Wang, Y. Kamiya, X. Wang, J. Ma, and Q. Zhang, Phys. Rev. B **103**, 035144 (2021).
[24] Z. Zhang, J. Li, M. Xie, W. Zhuo, D. T. Adroja, P. J. Baker, T. G. Perring, A. Zhang, F. Jin, J. Ji, X. Wang, J. Ma, and Q. Zhang, Phys. Rev. B **106**, 085115 (2022).
[25] J. Xing, L. D. Sanjeewa, J. Kim, G. Stewart, M.-H. Du, F. A. Reboredo, R. Custelcean, and A. S. Sefat, ACS Mater. Lett. **2**, 71 (2019).
[26] A. O. Scheie *et al.*, Nat. Phys. **20**, 74 (2024).
[27] See Supplemental Material at http://link.aps.org/supplemental/10.1103/PhysRevLett.133.266703 for crystal growth, x-ray and neutron diffraction, additional heat capacity, inelastic neutron scattering data, and their analysis, which include Ref. [28].
[28] Y. Ran, M. Hermele, P. A. Lee, and X.-G. Wen, Phys. Rev. Lett. **98**, 117205 (2007).
[29] S. Hu, W. Zhu, S. Eggert, and Y.-C. He, Phys. Rev. Lett. **123**, 207203 (2019).
[30] N. E. Sherman, M. Dupont, and J. E. Moore, Phys. Rev. B **107**, 165146 (2023).
[31] M. Drescher, L. Vanderstraeten, R. Moessner, and F. Pollmann, Phys. Rev. B **108**, L220401 (2023).
[32] Y. Zhou, K. Kanoda, and T.-K. Ng, Rev. Mod. Phys. **89**, 025003 (2017).
[33] Y.-D. Li and G. Chen, Phys. Rev. B **96**, 075105 (2017).
[34] Y. Shen, Y.-D. Li, H. C. Walker, P. Steffens, M. Boehm, X. Zhang, S. Shen, H. Wo, G. Chen, and J. Zhao, Nat. Commun. **9**, 4138 (2018).
[35] X.-G. Wen, Phys. Rev. B **65**, 165113 (2002).
[36] X.-Y. Song, C. Wang, A. Vishwanath, and Y.-C. He, Nat. Commun. **10**, 4254 (2019).
[37] F. Ferrari and F. Becca, Phys. Rev. X **9**, 031026 (2019).
[38] Y. Xu, J. Zhang, Y. S. Li, Y. J. Yu, X. C. Hong, Q. M. Zhang, and S. Y. Li, Phys. Rev. Lett. **117**, 267202 (2016).

[39] J. A. Mydosh, *Spin Glasses: An Experimental Introduction* (CRC Press, London, 1993).
[40] K. S. Cole and R. H. Cole, J. Chem. Phys. **9**, 341 (1941).
[41] K. Binder and A. P. Young, Rev. Mod. Phys. **58**, 801 (1986).
[42] E. Gopal, *Specific Heats at Low Temperatures* (Springer, Plenum Press, New York, 1966).
[43] R. Sarkar, P. Schlender, V. Grinenko, E. Haeussler, P. J. Baker, T. Doert, and H.-H. Klauss, Phys. Rev. B **100**, 241116(R) (2019).
[44] Z. Zhang, X. Ma, J. Li, G. Wang, D. T. Adroja, T. P. Perring, W. Liu, F. Jin, J. Ji, Y. Wang, Y. Kamiya, X. Wang, J. Ma, and Q. Zhang, Phys. Rev. B **103**, 035144 (2021).
[45] W. Steinhardt, P. Maksimov, S. Dissanayake, Z. Shi, N. P. Butch, D. Graf, A. Podlesnyak, Y. Liu, Y. Zhao, G. Xu *et al.*, npj Quantum Mater. **6**, 78 (2021).
[46] J. Gaudet, A. M. Hallas, C. R. C. Buhariwalla, G. Sala, M. B. Stone, M. Tachibana, K. Baroudi, R. J. Cava, and B. D. Gaulin, Phys. Rev. B **98**, 014419 (2018).
[47] Y.-Y. Pai, C. E. Marvinney, L. Liang, J. Xing, A. Scheie, A. A. Puretzky, G. B. Halász, X. Li, R. Juneja, A. S. Sefat, D. Parker, L. Lindsay, and B. J. Lawrie, J. Mater. Chem. C **10**, 4148 (2022).
[48] M. Christos, Z.-X. Luo, H. Shackleton, Y.-H. Zhang, M. S. Scheurer, and S. Sachdev, Proc. Natl. Acad. Sci. U.S.A. **120**, e2302701120 (2023).
[49] A. C. Hannon, Nucl. Instrum. Methods Phys. Res., Sect. A **551**, 88 (2005), proceedings of the E-MRS Fall Meeting 2004, Symposium D.
[50] G. Granroth, A. Kolesnikov, T. Sherline, J. Clancy, K. Ross, J. Ruff, B. Gaulin, and S. Nagler, J. Phys. Conf. Ser. **251**, 012058 (2010).
[51] G. Ehlers, A. A. Podlesnyak, J. L. Niedziela, E. B. Iverson, and P. E. Sokol, Rev. Sci. Instrum. **82**, 085108 (2011).
[52] Y. Iqbal, W.-J. Hu, R. Thomale, D. Poilblanc, and F. Becca, Phys. Rev. B **93**, 144411 (2016).
[53] A. Szasz, J. Motruk, M. P. Zaletel, and J. E. Moore, Phys. Rev. X **10**, 021042 (2020).
[54] S. R. White, Phys. Rev. Lett. **69**, 2863 (1992).
[55] U. Schollwöck, Ann. Phys. (Amsterdam) **326**, 96 (2011), January 2011 Special Issue.
[56] J. Haegeman, J. I. Cirac, T. J. Osborne, I. Pižorn, H. Verschelde, and F. Verstraete, Phys. Rev. Lett. **107**, 070601 (2011).
[57] J. Haegeman, T. J. Osborne, and F. Verstraete, Phys. Rev. B **88**, 075133 (2013).
[58] J. Haegeman, C. Lubich, I. Oseledets, B. Vandereycken, and F. Verstraete, Phys. Rev. B **94**, 165116 (2016).
[59] L. Vanderstraeten, J. Haegeman, and F. Verstraete, SciPost Phys. Lect. Notes 7 (2019).
[60] M. Yang and S. R. White, Phys. Rev. B **102**, 094315 (2020).

End Matter

Appendix A: Sample preparation and single-crystal growth—The polycrystalline sample of $YbZn_2GaO_5$ was synthesized using a solid-state reaction route. The high-purity precursors of Yb_2O_3 (99.9%), Ga_2O_3 (99.9%), and ZnO (99.9%) with 5% excess ZnO were used and mixed thoroughly and then pressed into a pellet. The pellets were sintered at 1275 °C for 36 h with intermediate grinding to obtain a pure phase of $YbZn_2GaO_5$. The phase purity is confirmed using powder x-ray diffraction (see Fig. S1). The pure powder sample and around 10% excess of ZnO were mixed and pressed into a cylindrical rod using a hydrostatic pressure of 700 bar. Single crystals of $YbZn_2GaO_5$ were grown using the optical floating-zone technique in the presence of a 10-bar oxygen atmosphere. A transparent single-grain crystal was successfully obtained, with a cleaved facet plane along [001] which was confirmed from Laue x-ray diffraction (see Fig. S1).

Appendix B: Single-crystal X-ray diffraction—The single-crystal x-ray diffraction is performed on $YbZn_2GaO_5$ single-crystal sample at the Department of Chemistry, University of North Carolina. A colorless transparent crystal piece (approximate dimensions $0.020 \times 0.010 \times 0.010$ mm^3) was harvested by an x-ray transparent loop made by MiTeGen and mounted on a Bruker D8 VENTURE diffractometer and measured at 150 K. The data collection was carried out using Mo-Kα radiation (graphite monochromator) with a frame time of 0.4 s and a detector distance of 4 cm.

Appendix C: AC susceptibility—The ac susceptibility experiments were carried out using two setups. The ac susceptibility χ' is measured in a dilution refrigerator attached to a Quantum Design Physical Property Measurement System (PPMS) Dynacool and the Cole-Cole plot (Argand diagram) is measured in the SCM1 at the National High Magnetic Field Laboratory. For the first experiment carried out in a PPMS, a piece of high-quality single crystal with a mass of 14 mg was used. The temperature-dependent χ' measurements were conducted from 1 to 0.055 K. For the National High Magnetic Field Laboratory measurements, four pieces of high-quality single-crystal samples, with a total mass of 25 mg, were coaligned and stacked together to enhance the signal. The samples were then placed inside a Kapton tube and secured with a small amount of super glue. The single crystals were carefully polished with sandpaper to achieve a close-to-1 filling factor within the tube, which can help achieve the optimal resolution. For the Cole-Cole analysis, a sequence of frequencies from 40 to 3000 Hz was used at different fixed temperatures.

Appendix D: Specific heat measurements—Specific heat measurements were carried out on single-crystal samples of $YbZn_2GaO_5$ and $LuZn_2GaO_5$ using a Helium-4 ($1.8\ \mathrm{K} \leq T \leq 300\ \mathrm{K}$) and dilution refrigerator ($0.05\ \mathrm{K} \leq T \leq 2\ \mathrm{K}$) setup attached to Quantum Design PPMS Dynacool. A representative single-crystal sample of $YbZn_2GaO_5$ mounted on a specific heat measurement platform is shown in the Supplemental Material (see Fig. S4).

Appendix E: Magnetic measurements—Temperature-dependent magnetic susceptibility was measured using a 7 Tesla Cryogenic Ltd superconducting quantum interference device magnetometer with a Helium-3 probe from 0.3 to 2 K and with a Helium-4 probe from 2 to 300 K. For the Helium-3 measurements, a small crystalline $YbZn_2GaO_5$ sample of 1.04 mg was mounted on a silver sample holder and for the Helium-4 measurement, 11.90 mg of $YbZn_2GaO_5$ single crystal was used. The crystals were oriented using the Laue diffraction method and the regular shape of the single crystals was obtained using a wire saw. The magnetic measurements were performed under an applied magnetic field parallel ($H\|$ c) and perpendicular ($H\perp$ c) to the crystallographic c directions of $YbZn_2GaO_5$. The isothermal magnetization measurements along both directions of $YbZn_2GaO_5$ single-crystal sample were performed using a vibration sample magnetometer in PPMS up to 14 Tesla of the applied magnetic field (see Fig. S1).

Appendix F: Neutron powder diffraction—Neutron powder diffraction measurement of $YbZn_2GaO_5$ was collected using the General Materials Diffractometer at the ISIS Neutron and Muon Source (Rutherford Appleton Laboratory, United Kingdom) [49]. The sample was loaded into an 8 mm diameter vanadium sample holder, and the neutron powder diffraction pattern was collected at room temperature, with a 15/40 mm (horizontal/vertical) beam size.

Appendix G: Inelastic neutron scattering—The inelastic neutron scattering experiments were performed on the Fine-Resolution Fermi Chopper Spectrometer [50] and the Cold Neutron Chopper Spectrometer [51] at the Spallation Neutron Source, Oak Ridge National Laboratory. For the Fine-Resolution Fermi Chopper Spectrometer experiment, 6.5 g of pure powder samples of $YbZn_2GaO_5$ and $LuZn_2GaO_5$ were used with incident neutron energies of $E_i = 80$ and 120 meV at temperatures of $T = 5$ and 100 K. The phonon contributions in the $YbZn_2GaO_5$ spectrum were subtracted using isostructural nonmagnetic $LuZn_2GaO_5$. For the Cold Neutron Chopper Spectrometer experiment, ten pieces of high-quality single-crystal samples of $YbZn_2GaO_5$ with a total mass of ~1.8 g were coaligned within 1.5° using a Laue x-ray backscattering diffractometer and mounted along $(hk0)$ scattering plane on an oxygen-free copper sample holder (see Fig. S1). The measurements were carried out in a dilution refrigerator with a base temperature of 0.1 K. A neutron-absorbing Cd foil was placed at the bottom of the holder to reduce the background from the sample holder. The measurements were conducted at the base temperature and 45 K under zero field with an incident neutron energy of $E_i = 3.32$ meV. The sample was rotated with an increment of 1°, with a range of −180° to 180°. The data were analyzed using the HORACE software and were folded three times along the high-symmetry axis $[0H0]$, $[\bar{H}H0]$, and $[H00]$ into a 60° sector in the reciprocal space to improve statistics. For the constant energy slice, the folded data were cut, duplicated, and recombined to restore 360° coverage for the purpose of presentation. To better extract the magnetic signal of interest, a comparative analysis was conducted between the 0.1 and 45 K spectra. The 45 K spectrum was normalized to 0.1 K data and used as background, which then was subtracted from the 0.1 K spectrum.

Appendix H: Theoretical calculations—We performed dynamical tensor network simulations of the $J_1 - J_2$ XXZ model on the triangular lattice, given by

$$H = J_1 \sum_{\langle i,j \rangle} (\Delta S_i^z S_j^z + S_i^x S_j^x + S_i^y S_j^y) \tag{H1}$$

$$+ J_2 \sum_{\langle\langle i,j \rangle\rangle} (\Delta S_i^z S_j^z + S_i^x S_j^x + S_i^y S_j^y), \tag{H2}$$

where S_i^α are spin-1/2 operators, and $\langle i,j \rangle$ and $\langle\langle i,j \rangle\rangle$ denote nearest- and next-nearest neighbor pairs, respectively. In this Letter, we only look at the value of $J_2/J_1 = 0.12$, which was chosen based on the similarity between the experimental spectra and the calculated spectra at this value reported in [30]. This value is believed to be deep in the QSL phase of the isotropic model [52]. To reflect some of the lowered symmetry in $YbZn_2GaO_5$, we add one anisotropy parameter Δ and study the Δ dependence; in principle, J_1 and J_2 could have different anisotropy parameters, and one could incorporate higher-order couplings as well, but the computational effort required to map the Brillouin zone for each choice of parameters means that we leave such further explorations for future work.

The quantity of interest is the dynamical structure factor, given by

$$S(\boldsymbol{q}, \omega) = \frac{1}{N} \sum_{\boldsymbol{x}} \int_0^\infty \frac{\mathrm{d}t}{2\pi} e^{i(\omega t - \boldsymbol{q}\cdot\boldsymbol{x})} G(\boldsymbol{x}, t), \tag{H3}$$

with N the number of lattice sites. The quantity $G(\boldsymbol{x}, t)$ is the two-point spin-spin correlation function defined as

$$G(\boldsymbol{x}, t) = \langle \Omega | \boldsymbol{S}_x(t) \cdot \boldsymbol{S}_c(0) | \Omega \rangle, \tag{H4}$$

where c denotes the center site of the lattice taken to be the origin, $\boldsymbol{x}$ is the distance of site $\boldsymbol{x}$ from the origin, and $|\Omega\rangle$ is the ground state of H with energy E_0. To calculate this quantity, we split the calculation into three parts by writing

$$\boldsymbol{S}_x \cdot \boldsymbol{S}_c = S_x^z S_c^z + \frac{1}{2}[S_x^+ S_c^- + S_x^- S_c^+]. \tag{H5}$$

To calculate $S(\boldsymbol{q}, \omega)$, we use the same method described in Ref. [30], but we will provide a summary of the technique here.

First, we curl the triangular lattice into a cylinder with a circumference $C = 6$, and a length $L = 36$, such that $N = LC$, using the XC boundary conditions [53]. Then, working with matrix product states, we calculate the ground state using the density matrix renormalization group [54,55]. The time evolution for $G(\boldsymbol{x}, t)$ is calculated using the

time-dependent variational principle [56–60], with a time step of 0.1, and maximum time $T_{\max} = 30$. We use a maximum bond dimension $\chi = 512$ for the simulations.

To smooth the data in frequency space, we rescale $G(\boldsymbol{x}, t)$ by a Gaussian. In particular

$$G(\boldsymbol{x}, t) \longrightarrow e^{-\eta t^2} G(\boldsymbol{x}, t), \tag{H6}$$

and we use $\eta = 0.02$ here. Since our system is inversion symmetric, we rewrite the Fourier transform in Eq. (H3) as

$$S(\boldsymbol{q}, \omega) = \frac{1}{\pi N} \int_0^\infty \mathrm{d}t \sum_{\boldsymbol{x}} \cos(\boldsymbol{q} \cdot \boldsymbol{x}) \times \Big(\cos(\omega t) \mathsf{Re} G(\boldsymbol{x}, t) - \sin(\omega t) \mathsf{Im} G(\boldsymbol{x}, t) \Big), \tag{H7}$$

yielding the results displayed here.

Lastly, due to a small circumference of the cylinder used during the simulations, this restricts the allowed wave vectors $\mathbf{q}$ to a subset of the full Brillouin zone. Since the infinite system has a full C_6 rotational symmetry, this means that the dynamical structure factor should have the same symmetry. In particular, in the thermodynamic limit, for any rotation $R \in C_6$, we have

$$S(R\boldsymbol{q}, \omega) = S(\boldsymbol{q}, \omega). \tag{H8}$$

We use this factor to generate the values $S(R\boldsymbol{q}, \omega)$ from the initial data $S(\boldsymbol{q}, \omega)$. For more details on the simulations, we point the reader to Ref. [30].